applied optics

Microlens array snapshot hyperspectral microscopy system for the biomedical domain

Changben Yu,[1,2] Jin Yang,[1] Nan Song,[1] Ci Sun,[1] Mingjia Wang,[1] and Shulong Feng[1,*]

[1]Changchun Institute of Optics, Fine Mechanics and Physics, Chinese Academy of Sciences, Changchun, Jilin 130033, China
[2]University of Chinese Academy of Sciences, Beijing 100049, China
*Corresponding author: topfsl@126.com

Received 21 December 2020; revised 29 January 2021; accepted 1 February 2021; posted 3 February 2021 (Doc. ID 417952); published 24 February 2021

We propose a microlens array-type snapshot hyperspectral microscope system that can provide spatial spectrum sampling according to detector frame rates for the biomedical domain. The system uses a shared optical path design. One path is used to perform direct microscopic imaging with high spatial resolution, while the other is used to collect microscopic images through a microlens array; the images are then spatially cut and reimaged such that they are spaced simultaneously by the prism-grating type hyperspectral imager's dispersion. Rapid acquisition of a three-dimensional data cube measuring 28 × 14 × 180 ($x \times y \times \lambda$) can be performed at the detector's frame rate. The system has a spatial resolution of 2.5 μm and can achieve 180-channel sampling of a 100 nm spectrum in the 400–800 nm spectral range with spectral resolution of approximately 0.56 nm. Spectral imaging results from biological samples show that the microlens array-type snapshot hyperspectral microscope system may potentially be applied in real-time biological spectral imaging.

https://doi.org/10.1364/AO.417952

1. INTRODUCTION

Optical microscopes are instruments used to perform observations in the microscopic range, and hyperspectral imagers are instruments used for the optical imaging and spectral analysis domains. When these two instruments are used together, they enable imaging of small areas while also providing a spectral analysis capability within these areas. This combined hyperspectral microscopy approach has been used widely in pharmaceutical research [1], materials science [2], biotechnology [3], mineral analysis [4], anticounterfeiting procedures for paper money [5], and other fields. In the biomedical field, the hyperspectral microscopy system can analyze important structures and measure the biochemical or physiological information contained in biological samples from the emission or reflection spectra of the biological sample [6] and from the fluorophores that can be used to distinguish spectral overlap [7,8], or can be applied to *in vivo* clinical diagnosis at the cell tissue level [9,10]. Common methods used to realize the addition of a spectral dimension to the dimensions of the two-dimensional image include the point-by-point scanning mode of the two-dimensional image dimensions [11], the one-dimensional line-by-line scanning mode through slits [12], use of digital light-processing methods [13], and use of an acousto-optic tunable filter [14] or a liquid crystal tunable filter [15] to scan in the spectral dimension.

The microspectroscopy system described above has to perform a lengthy scanning process when acquiring complete data cubes, which limits its application to fields including analysis of the biochemical reactions in living cells [16–18], chemical synthesis [18], and drug release [19]. However, with the latest developments in charge-coupled device (CCD) technology, a class of hyperspectral imagers called snapshot imagers has been developed. The term "snapshot" refers to the ability of these spectrometers to record the wavelength (λ) stack in just a single exposure of the camera [20]. These devices were first used in astronomy [21] and remote sensing [22] applications. The snapshot-type hyperspectral imager can be used to perform longer exposures in the dark or can be used to acquire images at higher speeds. This snapshot-type hyperspectral imager does not require a scanning action and can also eliminate motion artifacts in dynamic scenes [23]. The imager can thus reduce the need for high excitation energies to reduce the amount of photobleaching of the fluorophore [24].

Integral field spectroscopy (IFS) technology is a type of snapshot spectral imaging technology that uses a fiber array [25,26], a mirror array [27], or a microlens array [20] to segment and rearrange the microscopic part of the image to allow the CCD detector to record the two-dimensional spatial image and the spectral dispersion information simultaneously [28]. The fiber-array-based snapshot imaging spectrometer is based on a series of fiber bundles, with use of multiple spectrometers to observe

the full field of view, thus allowing snapshot spectral imaging to be achieved [29]. The mirror-array-based snapshot imaging spectrometer divides the entire field of view into segments using a series of micromirror arrays, but use of the mirror array brings problems that include processing difficulty, large amounts of stray light in practical applications, and low spectral resolution [27].

In this work, our team has designed a microlens-array-type snapshot hyperspectral microscope system. The system uses a shared optical path design. While one path is used to perform direct microscopic imaging with high spatial resolution, the other path is directed through a microlens array, which allows high-speed acquisition of the three-dimensional data cube measurements to be performed at the frame rate of the detector.

2. INSTRUMENT DESCRIPTION

A. Optical Layout

The optical layout of the proposed microlens-array-type snapshot hyperspectral microscope system is shown in Fig. 1. After the sample is magnified using a microscope objective lens (PLN100XOPH, Olympus) and a tube lens, the light is split using a beam splitter. One light beam is used to perform imaging with high spatial resolution, and the other beam is used to perform segmentation and sampling of the enlarged image obtained from the microscopic imaging part of the system through the microlens array. The microlens array condenses the high f-number (slow lens) light from the microscopic imaging part into low f-number (fast lens) light to form an array of microapertures that are separated from each other. The spatial position of each microaperture corresponds to the spatial position in the image sampled using the microlens array. These microaperture arrays are separated from each other; the degree of separation is determined by a combination of the microscopic imaging part and the microlens unit. The microaperture array formed by the convergence of the microlens array is collimated using the collimating lens of the prism-grating (PG)-type surface field-of-view hyperspectral imager, dispersed by the PG, and then converged via the focusing lens before being dispersed on the two-dimensional photodetector.

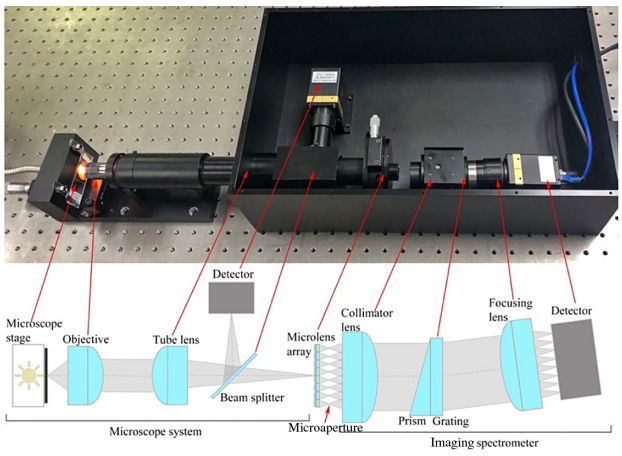

Fig. 1. Optical layout of the microlens-array-type snapshot hyperspectral microscope system.

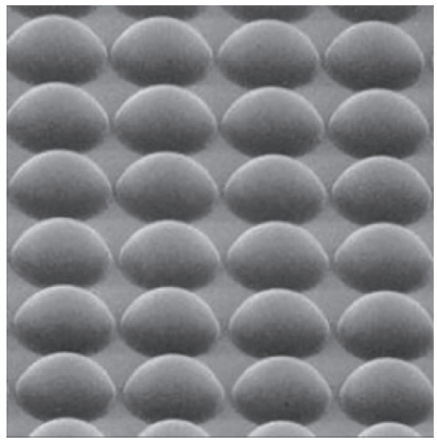

Fig. 2. Microlens array.

B. Analysis of the Microlens Array

As shown in Fig. 2, the microlens array is an array composed of lenses that each have a transparent aperture and a micrometer-scale relief depth. The array performs the basic focusing and imaging functions of traditional lenses and has a small unit size because of its high level of integration. A smaller center distance in the microlens unit leads to higher spatial resolution, and the spectral resolution then increases after the dispersion process of the hyperspectral imager; however, as the size of the microlens unit decreases, more spectral bands are then dispersed simultaneously on the rear CCD detector, and more closely spaced spectral bands leads to increasingly serious band overlap. Because the microlens unit is mostly composed of plano–convex lenses, chromatic aberrations occur during the focusing process. When only parallel light is incident along the optical axis, the minimum light aperture after the light is collected remains fixed. However, in practical applications, the front microscopic imaging section is designed to be an image-side telecentric system. When the telecentricity changes, the minimum clear aperture also changes, and interference may then occur between the microlens units. Therefore, it is necessary to analyze the interference relationships between the microlens units, the front microscopic imaging section, and the rear dispersion section.

In the microscopic imaging part of the system, a larger numerical aperture indicates a stronger ability to collect incident light. As shown in Fig. 3(a), when the image-side numerical aperture of the microscopic imaging section is too large, part of the light that should be concentrated behind the nth microlens unit is then concentrated behind an adjacent microlens unit, which will cause a difference in the interference that occurs in the spectral information acquired by the microlens unit. As shown in Fig. 3(b), when the image-side numerical aperture of the microscopic imaging section is reduced, each microlens unit n can converge all of the divided microscopic field of view into that microlens unit n, thus ensuring that the microscopic imaging area is enlarged and the resulting sample image does not include interference between the microlens units.

The discussion above indicates that it is important to avoid interference between the microlens units of the microscopic imaging part that are used to magnify the sample image. When designing the microscopic system for the snapshot dynamic hyperspectral imager, the microscopic imaging part of the

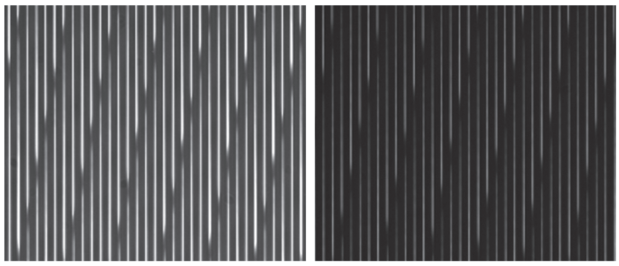

(a) (b)

Fig. 3. Schematic diagrams of interference. (a) Interference; (b) no interference.

imager should be designed to be an image-side telecentric system because it is necessary to limit both the image-side telecentricity and the image-side field angle of the microscopic imaging part simultaneously.

3. OPTICAL DESIGN OF THE MICROLENS-ARRAY-TYPE SNAPSHOT HYPERSPECTRAL MICROSCOPE SYSTEM

A. Optical Design of Microscopic Imaging Section

In this article, because of the long optical path length of the system, the microscopic imaging and dispersion sections of the system are described separately.

The optical structure of the microscopic imaging section is illustrated in Fig. 4. A microlens array from SUSS Co. was selected with an array size of 10 mm × 0 mm. The array material is SiO_2, the center distance of the microlens unit is 250 μm, and its radius of curvature is 297 μm. The grating constant d = 300 l/mm, the diffraction order is −1, the prism vertex angle $\beta = 10.4°$. The microscope objective was the PLN100XOPH (Olympus), which was used to form an infinity-type microscope objective image on the surface of the microlens array and ensure that the sample image magnified by the microscopic imaging section will not be subject to interference between the microlens units. We designed a tube lens structure composed of three lenses that is suitable for wavelengths ranging from 400 to 800 nm and has a focal length of 180 mm and telecentricity of 0.0012°.

The detailed design parameters for the microscopic imaging section are listed in Table 1.

Next, we analyze the limiting conditions for the field angle on the image side of the microscopic imaging section. Figure 5 shows a schematic diagram of the edge-incident light on the front image side of the telecentric microscopic imaging section. When the edge of the microlens array is placed on the image surface of the front microscopic imaging section, as illustrated in Fig. 5, the refracted ray MK′ that originates from the incident ray KM is located at the edge of the microaperture. Let θ be the angle of incidence of light ray KM, and let θ' be the refraction angle of the refracted light ray MK′. From the law of refraction, we know that

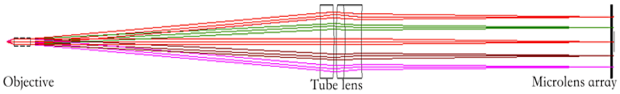

Fig. 4. Optical structure of the microscopic imaging section.

Table 1. Detailed Design Parameters for the Microscopic Imaging Section

Design Parameters	Parameter Value
Wavelength range/nm	400–800
Magnification	100×
Focal length (mm)	180
Image f-number	79
Detector pixel size/μm^2	7.4 × 7.4
Detector size/ mm^2	14.0 × 7

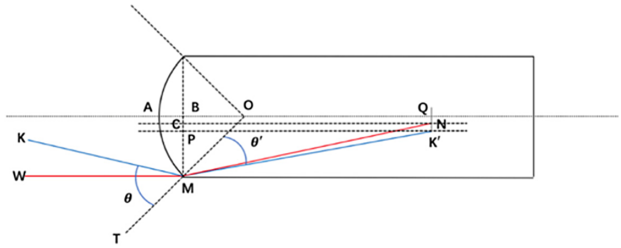

Fig. 5. Schematic diagram of edge-incident light on the surface of the microlens unit in the image-side telecentric microscopy imaging section.

$$n_0 \sin\theta = n_1 \sin\theta', \tag{1}$$

where n_0 is the refractive index of air and n_1 is the refractive index of fused silica. When only parallel light is incident along the optical axis, the center distance of the microlens unit is 250 μm, i.e., BM = 125 μm. The minimum spot size of a microlens array with a radius of curvature of OM = 297 μm is 22.9 μm after the chromatic spherical aberration is taken into account. QN = 11.45 μm represents half of the spot size. A hyperspectral imager with detector pixel dimensions of 7.4 μm × 7.4 μm and a magnification of 1 is selected for the analysis. To maximize the use of the CCD detector in the hyperspectral imager, it is assumed that the bandwidth of the spectral strip after the dispersion section of the hyperspectral imager is 4 pixels (29.6 μm). Therefore, the microaperture must be limited to 29.6 μm, i.e., the half-pore diameter QK′ = 14.8 μm. When simulated using optical design software, the distance between the microaperture and point A on the front surface of the microlens unit is AQ = 821.8 μm. This distance can be obtained using the following geometric relationship:

$$\theta = \arctan\left[\frac{(AQ - AO + \sqrt{OM^2 - BM^2})}{(BM - QK')}\right] - \arccos\left(\frac{BM}{OM}\right) \tag{2}$$

Substitution of Eq. (2) into Eq. (1) gives

$$\angle WMT = \arcsin\left\{\frac{n_1}{n_0}\sin\left[\arctan\left(\frac{(AQ - AO + \sqrt{OM^2 - BM^2})}{(BM - QN)}\right) - \arccos\left(\frac{BM}{OM}\right)\right]\right\}, \tag{3}$$

$$\angle KMW = \arcsin\left(\frac{n_1}{n_0}\sin\theta'\right) - \angle WMT \approx 0.36226°. \tag{4}$$

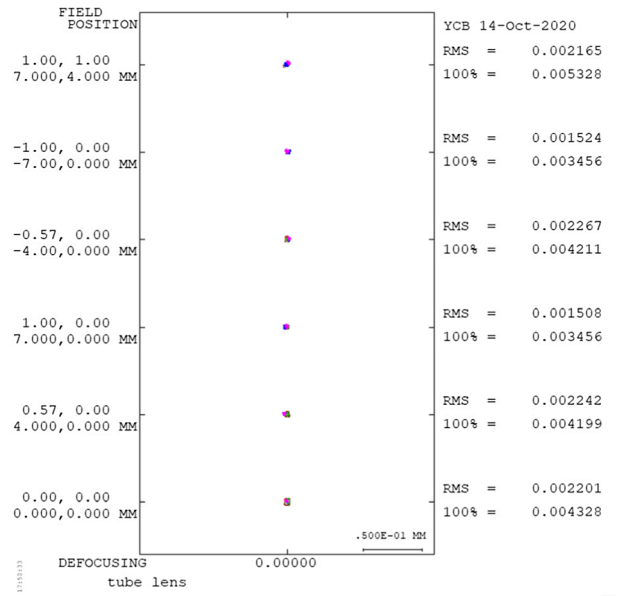

Fig. 6. Spot diagram of the microscopy imaging section.

Therefore, when the telecentricity of the tube lens is 0.0012°, the image-side f-number of the microscopic imaging section is given by

$$F_{\#} = \frac{1}{2}(n_0 \sin(\angle KMW - 0.0012°)) \approx 79.125 \quad (5)$$

At this time, the spot diagram of the microscopic imaging section is as shown in Fig. 6, and the spot size in each field of view is less than 5.4 μm.

B. Optical Design of PG Hyperspectral Imager with Large Aperture and Surface Field

In practical applications, the microlens condenses the high f-number (slow lens) light from the microscopic imaging section into low f-number (fast lens) light. The preceding analysis indicates that the spatial angle of incidence of the edge ray is 0.36226°, i.e., as in Fig. 7,

$$\angle WMD \approx 0.36226°, \quad (6)$$

$$\angle VXM = \frac{\pi}{2} - \arccos\left(\frac{BM}{OM}\right) - \arcsin\left[\frac{n_0}{n_1}\sin(\angle WMT - \angle WMD)\right]. \quad (7)$$

Therefore, the f-number of the hyperspectral imager behind the microlens array should be given by

$$F_{\#} = \frac{1}{2n_1 \sin\angle VXM} \approx 2.36. \quad (8)$$

The f-numbers of traditional reflective hyperspectral imagers cannot meet the requirements of snapshot hyperspectral microscopy systems based on microlens arrays. Therefore, we designed a transmission-type, large-aperture, surface-field-of-view hyperspectral imager system based on PG combined dispersion. The

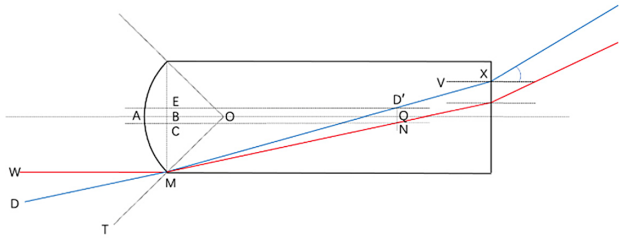

Fig. 7. Schematic diagram of microaperture edge-incident light.

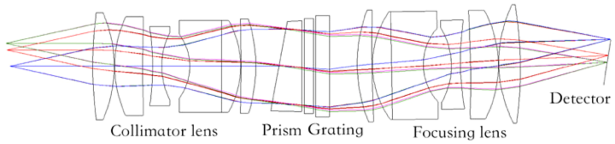

Fig. 8. Optical structure of PG hyperspectral imager with large aperture and surface field.

Table 2. Detailed Design Parameters for the Dispersion Section

Design Parameters	Parameter Value
Wavelength range/nm	400–800
Focal length /mm	37.6
f-number	2.36
Spectral resolution /nm	0.56
Detector pixel size/μm^2	7.4 × 7.4
Detector size/mm^2	14.0 × 7

optical structure of this system is illustrated in Fig. 8. The image surface of the microscopic imaging section is cut through the microlens array, which solves the overlap problem between the spatial information and the spectral information and realizes spectral imaging of the surface field of view. Because the prism and grating are in dispersion states, they cause the spectral line to bend in opposite directions; the system therefore adopts a combined form of dispersion for the prism and the grating that can correct the spectral line bending of the system appropriately.

The detailed design parameters for the dispersion section are presented in Table 2.

The spectroscopic system of the PG hyperspectral imager system with its large aperture and surface field adopts the PG structure and the front collimation system, and the rear imaging system use achromatic design, thus generating parallel light for transmission into the PG spectroscopic element and completing the secondary imaging process, respectively. The incident end of the dispersion section introduces a specific tilt into the dispersion direction to correct the spectral line curvature and color aberrations from the surface field-of-view dispersion and achieve high-quality imaging of the surface field of view. The optical modulation transfer function (MTF) curves of the PG hyperspectral imager with its large aperture and surface field at 400, 600, and 800 nm are shown in Fig. 9. The optical MTF of the complete wave band and the full field of view at the MTF cutoff position can reach 0.6. The system described above can meet the design requirements.

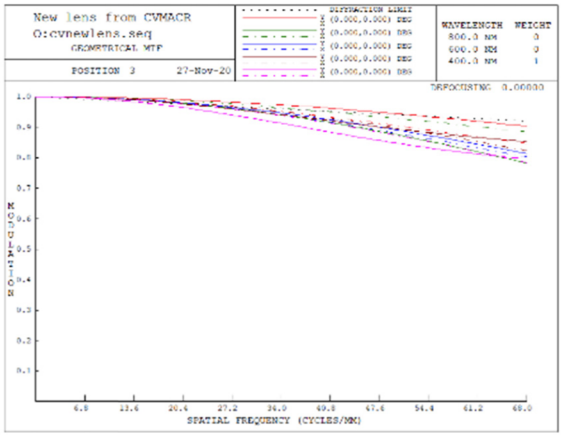

(a)

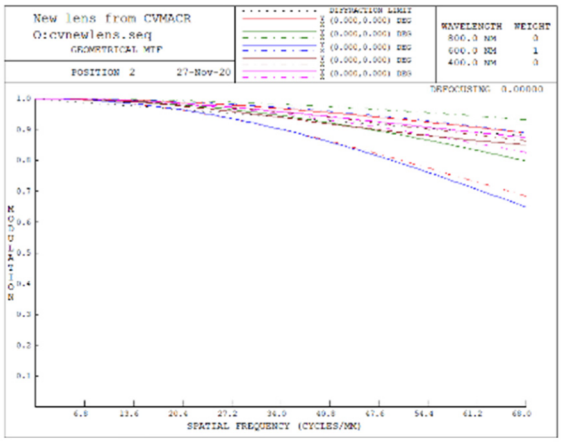

(b)

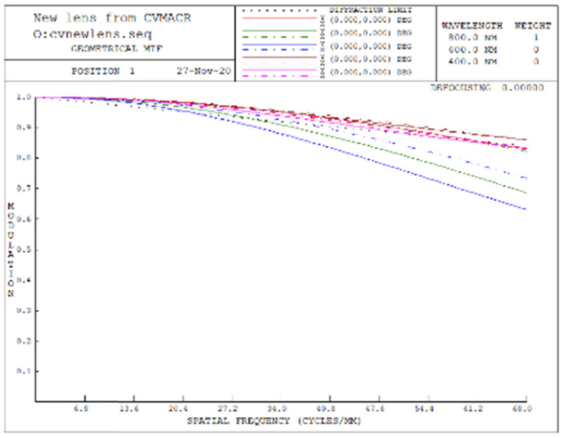

(c)

Fig. 9. MTF of the optical system of the PG hyperspectral imager at various wavelengths. (a) 400 nm; (b) 600 nm; (c) 800 nm.

4. IMAGING RESULTS

Figure 10 shows part of the original flat-field image captured by the detector that shows the spectrum of the illumination source (OSL2, Thorlabs). Rotation of the microlens array to an appropriate angle causes the interference between adjacent spectral bands to be eliminated. The flat-field image is used to correct the nonuniform intensity of the microlens array. To decode the spectral information and spatial information contained in the original image, we used mercury lamps to locate several single-wavelength positions and then used the three-dimensional spectral reconstruction algorithm model to locate the positions of the other wavelengths.

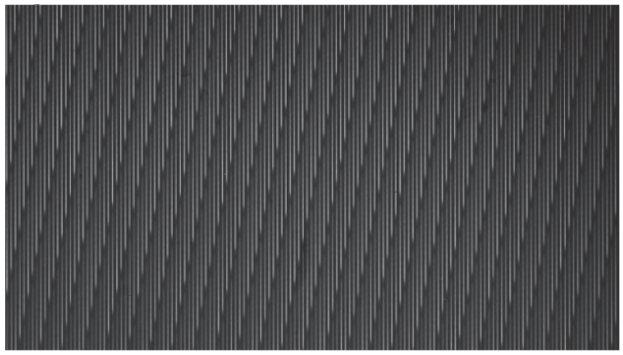

Fig. 10. Planar dispersion image of the microlens array.

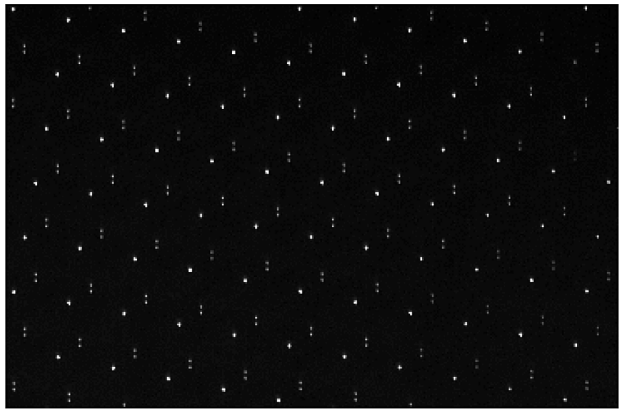

(a)

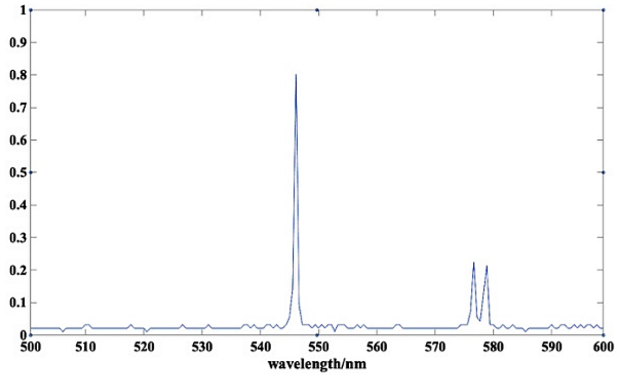

(b)

Fig. 11. Pixel image and acquired spectrum of the mercury lamps used. (a) Pixel image: spectral image of the mercury lamp; (b) intensity value: the mercury lamp spectrum extracted by the microlens unit.

The spectral image of the mercury lamp is shown in Fig. 11(a); the mercury lamp spectrum extracted by the microlens unit is shown in Fig. 11(b). Based on inversion calculations of the characteristic wavelengths of the mercury lamps at 546.075, 576.961, and 579.067 nm, an actual system resolution of 0.56 nm can be obtained.

We also performed experiments on gastric cancer samples at a snapshot speed of 50 ms to verify the spectral and spatial

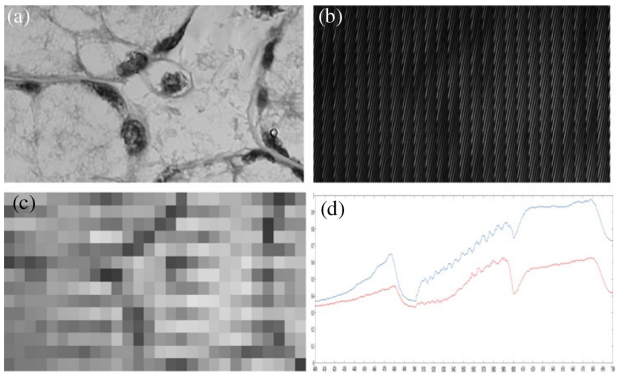

Fig. 12. Images and spectra acquired from the gastric cancer sample. (a) 500–600 nm direct gray-scale image of the gastric cancer samples; (b) 500–600 nm microlens array surface dispersion spectrum of the gastric cancer samples; (c) reconstructed single-channel image (at 546.075 nm) of a gastric cancer sample; (d) 400–700 nm spectra of the gastric cancer (red) cells and normal (blue) tissue cells, the significant differences in the absorption spectrum of the gastric cancerous tissue sample when compared with the characteristics of the normal tissue absorption spectrum.

resolution capabilities of the system. Figure 12(a) shows a 500–600 nm direct gray-scale image of the gastric cancer samples, and Fig. 12(b) shows the 500–600 nm microlens array surface dispersion spectrum of these gastric cancer samples. Figure 12(c) shows a reconstructed single-channel image (at 546.075 nm) of a gastric cancer sample. Because of the limitations between the spatial resolution and the spectral resolution, the system presented in this article can perform 180-channel spatial dispersion on a spectrum with a bandwidth of 100 nm in a single shot. Figure 12(d) shows the absorption spectra of the gastric cancer cells and normal tissue cells obtained by switching the filters used; these spectra contain spectral features between 400 and 700 nm and illustrate the significant differences in the absorption spectrum of the gastric cancerous tissue sample (red) when compared with the characteristics of the normal tissue absorption spectrum (blue).

5. CONCLUSIONS AND DISCUSSION

This article presents a microlens-array-type snapshot hyperspectral microscope system. We produced an integrated portable design for the proposed system. While one system path is used to perform direct microscopic imaging with high spatial resolution, the second path can perform high-speed acquisition of three-dimensional data cube measurements at the frame rate of the detector. The system has a spatial resolution of 2.5 μm and can achieve 180-channel spectral sampling of a 100 nm spectrum within the 400–800 nm spectral range with a spectral resolution of approximately 0.56 nm. In the experiments, because of detector size limitations, we used only a 28 × 14 microlens array, but we will expand this array size in the future. We have presented the design results and have tested the imaging performance of the designed system. The spectral imaging results obtained in biological samples indicate that the microlens-array-based snapshot microscopy system presented here has great potential for use in the field of real-time biological imaging research.

Funding. Department of Science and Technology of Jilin Province (20180201049SF, 20190201304JC, 20200403009SF); National Natural Science Foundation of China (61805240); Jilin Province Development and Reform Commission (2019C038-4); Jilin Province Special Funds for High-tech Industrialization in cooperation with the Chinese Academy of Sciences (CAS) (2020SYHZ0030, 2020SYHZ0034).

Disclosures. The authors declare no conflicts of interest.

REFERENCES

1. U. Maeder, K. Marquardt, S. Beer, T. Bergmann, T. Schmidts, J. T. Heverhagen, K. Zink, F. Runkel, and M. Fiebich, "Evaluation and quantification of spectral information in tissue by confocal microscopy," J. Biomed. Opt. **17**, 1060111 (2012).
2. J. Li, H. Li, H. Hu, Y. Zhao, and Q. Wang, "Preparation and spectral characteristics of silver nano-sphere doped quartz micro-fiber," Opt. Laser Technol. **68**, 79–83 (2015).
3. I. Egea, W. Bian, C. Barsan, A. Jauneau, J.-C. Pech, A. Latché, Z. Li, and C. Chervin, "Chloroplast to chromoplast transition in tomato fruit: spectral confocal microscopy analyses of carotenoids and chlorophylls in isolated plastids and time-lapse recording on intact live tissue," Ann. Bot. **108**, 291–329 (2011).
4. J. Tao, "FTIR and Raman studies of structure and bonding in mineral and organic-mineral composites," Methods Enzymol. **532**, 533–556 (2013).
5. A. Guedes, M. Algarra, A. Carmelo Prieto, B. Valentim, V. Hortelano, S. Neto, R. Algarra, and F. Noronha, "Raman microspectroscopy of genuine and fake Euro banknotes," Spectrosc. Lett. **46**, 569–576 (2013).
6. L. Gao, R. T. Kester, N. Hagen, and T. S. Tkaczyk, "Snapshot image mapping spectrometer (IMS) with high sampling density for hyperspectral microscopy," Opt. Express **18**, 14330–14344 (2010).
7. T. Zimmermann, J. Rietdorf, and R. Pepperkok, "Spectral imaging and its applications in live cell microscopy," FEBS Lett. **546**, 87–92 (2003).
8. Y. Hiraoka, T. Shimi, and T. Haraguchi, "Multispectral imaging fluorescence microscopy for living cells," Cell Struct. Funct. **27**, 367–374 (2002).
9. T. Vo-Dinh, "A hyperspectral imaging system for in vivo optical diagnostics," IEEE Eng. Med. Biol. Mag. **23**(5), 40–49 (2007).
10. J. Zuzak Karel, P. Francis Robert, F. Wehner Eleanor, S. Jack, L. Maritoni, W. Allen David, T. Chad, C. Jeffrey, and L. Edward, "Hyperspectral imaging utilizing LCTF and DLP technology for surgical and clinical applications," Proc. SPIE **7170**, 71700C (2009).
11. M. C. Pedroso, M. B. Sinclair, H. D. T. Jones, and D. M. Haaland, "Hyperspectral confocal fluorescence microscope: a new look into the cell," Microsc. Microanal. **15**, 880–881 (2009).
12. C. Sun, M. Wang, J. Cui, X. Yao, and J. Chen, "Comparison and analysis of wavelength calibration methods for prism-grating imaging spectrometer," Results Phys. **12**, 143–146 (2019).
13. K. J. Zuzak, R. P. Francis, E. F. Wehnerm, J. Smith, M. Litorja, D. W. Allen, C. Tracy, J. Cadeddu, and E. Livingston, "DLP hyperspectral imaging for surgical and clinical utility," Proc. SPIE **7210**, 721006 (2009).
14. P. M. Kasili and T. Vo-Dinh, "Hyperspectral imaging system using acousto-optic tunable filter for flow cytometry applications," Cytometry Part A **69A**, 835–841 (2006).
15. R. Lansford, G. Bearman, and S. E. Fraser, "Resolution of multiple green fluorescent protein color variants and dyes using two-photon microscopy and imaging spectroscopy," J. Biomed. Opt. **6**, 311–318 (2001).
16. K. N. Richmond, S. Burnite, and R. M. Lynch, "Oxygen sensitivity of mitochondrial metabolic state in isolated skeletal and cardiac myocytes," Am. J. Physiol. **273**, C1613–C1622 (1997).
17. R. Martínez-Zaguilán, M. W. Gurulé, and R. M. Lynch, "Simultaneous measurement of intracellular pH and Ca2+ in insulin-secreting cells by spectral imaging microscopy," Am. J. Physiol. **270**, 1438–1446 (1996).

18. Y. Li, B. Lin, L. Ge, H. Guo, X. Chen, and M. Lu, "Real-time spectroscopic monitoring of photocatalytic activity promoted by graphene in a microfluidic reactor," Sci. Rep. **6**, 28803 (2016).
19. A. Pestieau, F. Krier, G. Thoorens, A. Dupont, P.-F. Chavez, E. Ziemons, P. Hubert, and B. Evrard, "Towards a real time release approach for manufacturing tablets using NIR spectroscopy," J. Pharm. Biomed. Anal. **98**, 60–67 (2014).
20. J. G. Dwight and T. S. Tkaczyk, "Lenslet array tunable snapshot imaging spectrometer (LATIS) for hyperspectral fluorescence microscopy," Biomed. Opt. Express **8**, 1950–1964 (2017).
21. S. William and F. Holland, "Imaging spectroscopy for extrasolar planet detection," Astrophys. J. **578**, 543–564 (2002).
22. G. Vane, R. O. Green, T. G. Chrien, H. T. Enmark, E. G. Hansen, and W. M. Porter, "The airborne visible/infrared imaging spectrometer (AVIRIS)," Remote Sens. Environ. **44**, 127–143 (1993).
23. H. Nathan and W. Kudenov Michael, "Review of snapshot spectral imaging technologies," Opt. Eng. **52**, 090901 (2013).
24. V. Magidson and A. Khodjakov, "Circumventing photodamage in live-cell microscopy," Methods Cell Biol. **114**, 545–560 (2013).
25. Y. Wang, J. Gawedzinski, M. E. Pawlowski, and T. S. Tkaczyk, "3D printed fiber optic faceplates by custom controlled fused deposition modeling," Opt. Express **26**, 15362–15376 (2018).
26. Y. Murakami, K. Nakazaki, and M. Yamaguchi, "Hybrid-resolution spectral video system using low-resolution spectral sensor," Opt. Express **22**, 20311–20325 (2014).
27. L. Gao, R. Kester, and T. Tkaczyk, "Optical design of a snapshot high-sampling image mapping spectrometer (IMS) for hyperspectral microscopy," Proc. SPIE **7570**, 75700Z (2010).
28. Z. Zhang, J. Chang, H. Ren, K. Fan, and D. Li, "Snapshot imaging spectrometer based on a microlens array," Chin. Opt. Lett. **17**, 011101 (2019).
29. Y. Wang, M. E. Pawlowski, and T. S. Tkaczyk, "Light-guide snapshot spectrometer for biomedical applications," Proc. SPIE **9711**, 97111J (2016).